arXiv:1610.05993v1 [cond-mat.quant-gas] 19 Oct 2016

Maxwell Quasiparticles Emerged in Optical Lattices

Yan-Qing Zhu,[1] Dan-Wei Zhang,[2,*] Hui Yan,[2] Ding-Yu Xing,[1,3] and Shi-Liang Zhu[1,4,†]

[1]*National Laboratory of Solid State Microstructures and School of Physics, Nanjing University, Nanjing 210093, China*
[2]*Guangdong Provincial Key Laboratory of Quantum Engineering and Quantum Materials, SPTE, South China Normal University, Guangzhou 510006, China*
[3] *Collaborative Innovation Center of Advanced Microstructures, Nanjing 210093, China*
[4]*Synergetic Innovation Center of Quantum Information and Quantum Physics, University of Science and Technology of China, Hefei, Anhui 230026, China*

(Dated: October 20, 2016)

We construct a two-dimensional tight-binding model of an optical lattice, where the low energy excitations should be described by the spin-1 Maxwell equations in the Hamiltonian form, and such linear dispersion excitations with pesudospin-1 are so called as the Maxwell quasiparticles. The system has rich topological features, for examples, the threefold degeneracy points called Maxwell points may have nontrivial $\pm 2\pi$ Berry phases and the anomalous quantum Hall effect with spin-momentum locking may appear in topological Maxwell insulators. We propose realistic schemes for realizing the Maxwell metals/insulators and detecting the intrinsic properties of the topological Maxwell quasiparticles with ultracold atoms in optical lattices.

Introduction.— Discovery of new particles in nature or new quasiparticles in condensed matter systems lies at the heart of the modern physics [1]. One of the recnet examples is that the relativistic Dirac fermions emerged in a graphene have attracted interest in condensed matter physics as well as in quantum field theory [2]. Furthermore, it was demonstrated that Weyl fermions, the massless spin-1/2 particles in quantum field theory but have never been observed as fundamental particles in nature, can emerge as quasiparticles in solids [3–5] and photonic crystals [6]. Most interestingly, the Dirac and Weyl fermions have rich topological features [3–8]. However, the quasiparticles with higher spin numbers that are also fundamentally important are rarely studied [9, 10]. For instance, the massless photons with spin-1 are fundamental particles in nature, which are described by Maxwell equations. Note that the Dirac and Weyl fermions have already been well investigated in the field of the cold atoms [11–16]. A natural question is raised: can we realize the Maxwell quasiparticles (relativistic excitations with pesudospin-1) with a well-designed ultracold atomic system?

In this Letter, we propose schemes to create and explore Maxwell quasiparticles in a two-dimensional (2D) optical lattice (OL). We first rewrite the Maxwell equations in an anisotropic medium in the form of the Schrödinger equation and then construct 2D optical lattices, where the low energy excitations should be described by the Maxwell Hamiltonian. By tuning the on-site spin-flip parameter, we show that the system can have rich quantum phases: topological or normal Maxwell insulator, topological or normal Maxwell metal. The topological Maxwell metal is characterized with the threefold degeneracy points, the so-called Maxwell points, which have nontrivial $\pm 2\pi$ Berry phases. The low-energy excitations near the Maxwell point behave like photons described by the Maxwell equations in the form of the Schrödinger equation. Furthermore, we find nontrivial edge states with spin-momentum locking in the topological Maxwell insulating phases, mimicking the circularly-polarized photons. Our work reveals the topological properties of Maxwell quasiparticles, which are analogy with the Dirac and Weyl fermions in topological insulators and topological semimetals.

Maxwell equations in the form of the Schrödinger equation.— In a region in the absence of free charges and currents, the well-known Maxwell equations in matter are given by

$$\begin{aligned} \nabla \times \mathbf{E} &= -\frac{\partial \mathbf{B}}{\partial t}, \quad \nabla \cdot \mathbf{E} = 0, \\ \nabla \times \mathbf{H} &= \frac{\partial \mathbf{D}}{\partial t}, \quad \nabla \cdot \mathbf{B} = 0, \end{aligned} \tag{1}$$

where the displacement field $\mathbf{D} = \varepsilon_0 \varepsilon_r \mathbf{E}$ with $\mathbf{E}$ being the electric field, the magnetic field $\mathbf{B} = \mu_0 \mu_r \mathbf{H}$ with $\mathbf{H}$ being the magnetizing field, ε_r and μ_r are the relative permittivity and permeability, respectively. In an anisotropic medium, ε_r and μ_r are tensors rather than numbers. To simplify the proceeding analysis, we assume that the tensors ε_r and μ_r are simultaneously diagonalized. We can define the photon wave function as $\mathbf{\Phi}(\mathbf{r}, t) = \tilde{\mathbf{E}}(\mathbf{r}, t) + i\tilde{\mathbf{H}}(\mathbf{r}, t)$ [1, 2], where $\tilde{E}_\alpha = \sqrt{\varepsilon_0 \varepsilon_\alpha} E_\alpha$ and $\tilde{H}_\alpha = \sqrt{\mu_0 \mu_\alpha} H_\alpha$. Then the Maxwell equations can be rewritten as $\nabla \cdot \mathbf{\Phi} = 0$ and $i\hbar \frac{\partial \Phi^\alpha}{\partial t} = \nu_{\alpha\gamma}(i\epsilon_{\alpha\beta\gamma}) \hat{P}_\beta \frac{\partial \Phi^\gamma}{\partial \beta}$, where $\nu_{\alpha\gamma} = c/\sqrt{\varepsilon_\alpha \mu_\gamma}$, $\hat{P}_\beta = -i\hbar\partial_\beta$, and $\epsilon_{\alpha\beta\gamma}$ ($\alpha, \beta, \gamma = x, y, z$) is the Levi-Civita symbol. We can rewrite the Maxwell equations in the form of the Schrödinger's equation as $i\hbar \frac{\partial}{\partial t} \mathbf{\Phi} = \hat{H}_M \mathbf{\Phi}$ where the Maxwell Hamiltonian of the photons is given by [19]

$$\hat{H}_M = v_x \hat{S}_x \hat{P}_x + v_y \hat{S}_y \hat{P}_y + v_z \hat{S}_z \hat{P}_z. \tag{2}$$

Here $\hat{\mathbf{S}} = (\hat{S}_x, \hat{S}_y, \hat{S}_z)$ are the spin matrices for a particle of spin-1 [19]. Equation (2) is analogous to the Dirac

(Weyl) equation for the massless relativistic fermions with spin-1/2. In this paper, we demonstrate that the low-energy physics in some well-designed OLs loaded with free fermions (bosons) should be described by the Schrödinger equation with the Maxwell Hamiltonian (2), and thus we call such quasiparticles as the Maxwell fermions (bosons).

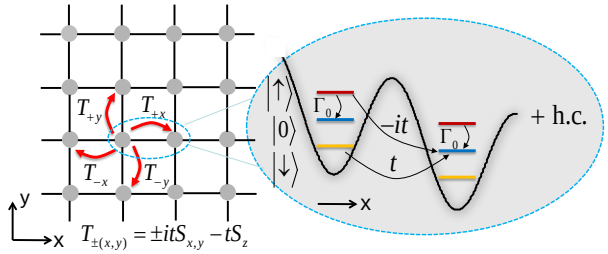

FIG. 1: (color online). Schematic diagram of realizing the 2D Maxwell lattices. The model Hamiltonian (S.13) can be realized with ultra-cold atoms loaded in a square OL with the spin-flip hopping $T_{\pm(x,y)}$ and on-site spin-flip term Γ_0. The three atomic internal states $|\uparrow\rangle, |0\rangle, |\downarrow\rangle$ form the (pseudo)spin-1 basis and the required atomic spin-flip hopping, such as T_{+x} shown on the right, can be engineered by Raman lasers.

The model.— The Maxwell quasiparticles can be realized with two different schemes. We can use non-interacting fermionic or bosonic atoms in a square OL and choose three atomic internal states in the ground state manifold to encode the three spin states $|s\rangle$ ($s = \uparrow, 0, \downarrow$). Alternatively, it can be realized by using single-component atoms in OLs with three sublattices, where the pseudospin-1 basis are replaced by the three sublattices A, B, C in a unit cell. The detailed schemes are addressed in Supplemental Materials [19]. For the conceptual simplicity, we discuss the formal one in the main text. The model Hamiltonian we considered is given by

$$\hat{H} = t\sum_{\mathbf{r}}\left[\hat{H}_{\mathbf{rx}} + \hat{H}_{\mathbf{ry}} + \left(\Gamma_0\hat{a}^{\dagger}_{\mathbf{r},0}\hat{a}_{\mathbf{r},\uparrow} + \text{H.c.}\right)\right], \qquad (3)$$

where $\hat{H}_{\mathbf{rx}} = -\hat{a}^{\dagger}_{\mathbf{r}-\mathbf{x},0}(\hat{a}_{\mathbf{r},\downarrow} + i\hat{a}_{\mathbf{r},\uparrow}) + \hat{a}^{\dagger}_{\mathbf{r}+\mathbf{x},0}(\hat{a}_{\mathbf{r},\downarrow} - i\hat{a}_{\mathbf{r},\uparrow}) +$ H.c. and $\hat{H}_{\mathbf{ry}} = \hat{a}^{\dagger}_{\mathbf{r}-\mathbf{y},\uparrow}(\hat{a}_{\mathbf{r},\downarrow} + i\hat{a}_{\mathbf{r},0}) - \hat{a}^{\dagger}_{\mathbf{r}+\mathbf{y},\uparrow}(\hat{a}_{\mathbf{r},\downarrow} - i\hat{a}_{\mathbf{r},0}) +$ H.c. respectively represent the spin-flip hopping along the x and y axis with the tunneling amplitude t, $\hat{a}_{\mathbf{r},s}$ is the annihilation operator on site $\mathbf{r}$ for the spin state $|s\rangle$, and $\Gamma_0 = 2iM$ with the tunable parameter M being the strength of the on-site spin-flip. The required spin-flip hopping and on-site spin-flip terms are demonstrated in Fig. 1. The spin-flip hopping terms $\hat{H}_{\mathbf{rx}}$ and $\hat{H}_{\mathbf{ry}}$ can be achieved by the Raman-assisted tunneling scheme [3–5, 21, 22] with Raman lasers, which address atoms with the laser-frequency and polarization selections [19]. The on-site spin-flip term $\Gamma_0\hat{a}^{\dagger}_{\mathbf{r},0}\hat{a}_{\mathbf{r},\uparrow}$ can be achieved and tuned by application of a simple radio-frequency field or additional Raman beams.

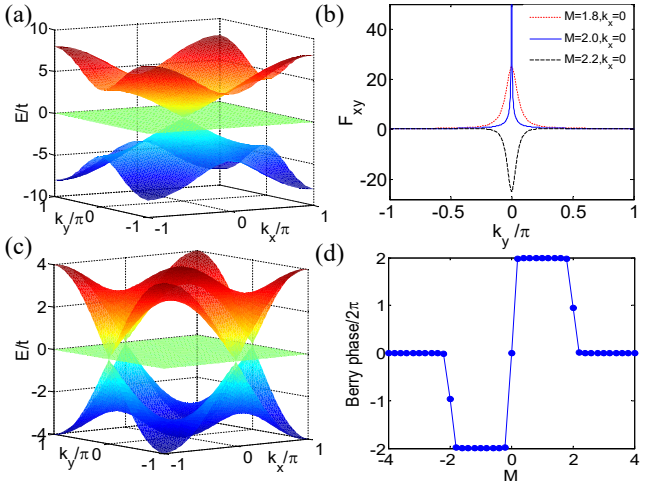

FIG. 2: (color online). The energy spectra and topological features of the 2D Maxwell lattices. (a) The energy spectrum for $M = 2$; (b) The Berry curvature $F_{xy}(k_y)$ for $k_x = 0$ and $M = 1.8, 2, 2.2$; (c) The energy spectrum for $M = 0$; (d) The Berry phase γ as a function of the parameter M, which corresponds to the Chern number $\mathcal{C}_1 = \gamma/2\pi$ when the 2D system is in the insulating phase with $M \neq 0, \pm 2$.

Under the periodic boundary condition, the model Hamiltonian (S.13) can be rewritten as $\hat{H} = \sum_{\mathbf{k},ss'}\hat{a}^{\dagger}_{\mathbf{k}s}[\mathcal{H}(\mathbf{k})]_{ss'}\hat{a}_{\mathbf{k}s'}$, where $\hat{a}_{\mathbf{k}s} = 1/\sqrt{V}\sum_k e^{i\mathbf{k}\cdot\mathbf{r}}\hat{a}_{\mathbf{k}s}$ is the annihilation operator in momentum space $\mathbf{k} = (k_x, k_y)$, and $\mathcal{H}(\mathbf{k}) = \mathbf{R}(\mathbf{k})\cdot\hat{\mathbf{S}}$ is the Bloch Hamiltonian. Here $\mathbf{R}(\mathbf{k}) = (R_x, R_y, R_z)$ denotes the Bloch vectors: $R_x = 2t\sin k_x, R_y = 2t\sin k_y$, and $R_z = 2t(M - \cos k_x - \cos k_y)$, with the lattice spacing $a \equiv 1$ and $\hbar \equiv 1$ hereafter. The energy spectrum of this system is given by $E(\mathbf{k}) = 0, \pm|\mathbf{R}(\mathbf{k})|$, which has a zero-energy flat band in the middle of the three bands.

Maxwell quasiparticles in Maxwell metals.— The three bands $E(\mathbf{k}) = 0, \pm|\mathbf{R}(\mathbf{k})|$ touch at one point when $M = \pm 2$, and touch at two points when $M = 0$. For the case $M = 2$, the three bands touch at $\mathbf{K}_+ = (0, 0)$ in the energy spectrum shown in Fig. 2(a). We expand the Bloch Hamiltonian near this threefold degenerate point and obtain the following effective Hamiltonian for the low-energy excitations in the system

$$\mathcal{H}_+(\mathbf{q}) = vq_x\hat{S}_x + vq_y\hat{S}_y, \qquad (4)$$

where $v = 2t$ is the effective speed of light and $\mathbf{q} = \mathbf{k} - \mathbf{K}_+$. This effective Hamiltonian takes the Maxwell Hamiltonian $\hat{H}_{\text{M}}$ in two dimensions and thus the dynamics of the low-energy excitations can be effectively described by the Maxwell Hamiltonian (2). In this sense, we name these low-energy excitations as the Maxwell quasiparticles and the threefold degeneracy point as the Maxwell point. When the ultra-cold atoms are fermions and the Fermi level lies near the Maxwell point, the system can be named as the Maxwell metals, which is a

metallic state due to the existence of the zero-energy flat band.

To study the topological stability of the Maxwell point, we consider the Berry phase for a Maxwell quasiparticle circling around the point $\gamma = \oint_c d\mathbf{k} \cdot \mathbf{F}(\mathbf{k})$, where the Berry curvature $\mathbf{F}(\mathbf{k}) = \nabla \times \mathbf{A}(\mathbf{k})$ with the Berry connection defined by the wave function $|\psi_n(\mathbf{k})\rangle$ in the n-th $(n = 1, 2, 3)$ band $\mathbf{A}(\mathbf{k}) = -i\langle\psi_n(\mathbf{k})|\nabla_{\mathbf{k}}|\psi_n(\mathbf{k})\rangle$. For this three-band system described by the Bloch Hamiltonian $\mathcal{H}(\mathbf{k})$, the lowest-band Berry curvature in the k_x-k_y space can be rewritten as [25]

$$F_{xy} = -\frac{1}{R^3}\mathbf{R} \cdot (\partial_{k_x}\mathbf{R} \times \partial_{k_y}\mathbf{R}). \tag{5}$$

The distributions of $F_{xy}(k_y)$ for fixed $k_x = 0$ and typical parameters $M = 1.8, 2, 2.2$ are plotted in Fig. 2(b), and the results show that F_{xy} is a Dirac-δ function at the Maxwell point. The numerical integration of F_{xy} over the Brillouin zone for $M = 2$ gives the Berry phase $\gamma = 2\pi$, which is confirmed by the analytical calculation [19].

For the case $M = -2$, the single Maxwell point moves to the Brillouin edge $\mathbf{K}_- = (\pi, \pi)$ with the Berry phase $\gamma = -2\pi$, and the low-energy effective Hamiltonian becomes $\mathcal{H}_-(\mathbf{q}) = -\mathcal{H}_+(\mathbf{q})$. When $M = 0$ with the energy spectrum shown in Fig. 2(c), there are two Maxwell points at $(0, \pi)$ and $(\pi, 0)$ with the effective Hamiltonian $\mathcal{H}_0(\mathbf{q}) = \pm v q_x \hat{S}_x \mp v q_y \hat{S}_y$, respectively. In this case, the Berry phase for both of the two Maxwell points is obtained as $\gamma = 0$, which corresponds to a trivial metallic state.

Maxwell edge modes in Maxwell insulators.— When the parameter $M \neq 0, \pm 2$, the two band gaps are open and the system becomes insulating states. Under this condition, we can calculate the Chern number $\mathcal{C}_n$ for the corresponding three bands with the band index n:

$$\mathcal{C}_n = \frac{1}{2\pi}\int_{BZ} dk_x dk_y F_{xy}(k_x, k_y) = \gamma/2\pi. \tag{6}$$

We find nonzero Chern numbers $\mathcal{C}_1 = -\mathcal{C}_3 = 2\text{sign}(M)$ for $|M| < 2$ and $\mathcal{C}_1 = \mathcal{C}_3 = 0$ for $|M| > 2$ [19], and thus $\mathcal{C}_2(M) = 0$ for the flat band. Figure 2(d) shows the Berry phase of the lowest band $\gamma = 2\pi\mathcal{C}_1$ as a function of the parameter M, which indicates that this system is subjected to three topological phase transitions at the tunable parameter $M = 2, 0, -2$.

To further study the topological properties of the system, we numerically calculate the energy spectrum of a cylindrical surface with periodic boundary condition for y direction and the length $L_x = 40$ under the open boundary condition along the x direction, and the results are shown in Fig. 3. From Figs. 3(a-e), we show the variation of the energy spectra by changing the parameter M. For $M = 4$ in Fig. 3(a), there is no edge mode in the two band gaps in this trivial insulating state with the Chern number $\mathcal{C}_n = 0$. Decreasing the parameter $|M|$ at critical values $M = \pm 2$ [Figs. 3(b) and 3(e)], the band gaps close and the system is in the nontrivial Maxwell metallic phase with $\pm 2\pi$ Berry phase (corresponding to the Chern number ± 1) and a branch of edge modes connecting the lowest (third) band and the middle flat band [19]. For $M = \pm 1$ [Figs. 3(c) and 3(d)], the spectra contain two pairs asymmetric branches of edge modes connecting the separated lowest (third) band and the middle flat band, which is consistent with bulk-edge correspondence in these cases with the bulk Chern number $|\mathcal{C}_{1,3}| = 2$. The density distributions of some edge modes are shown in the inset in Fig. 3(c) for typical k_y.

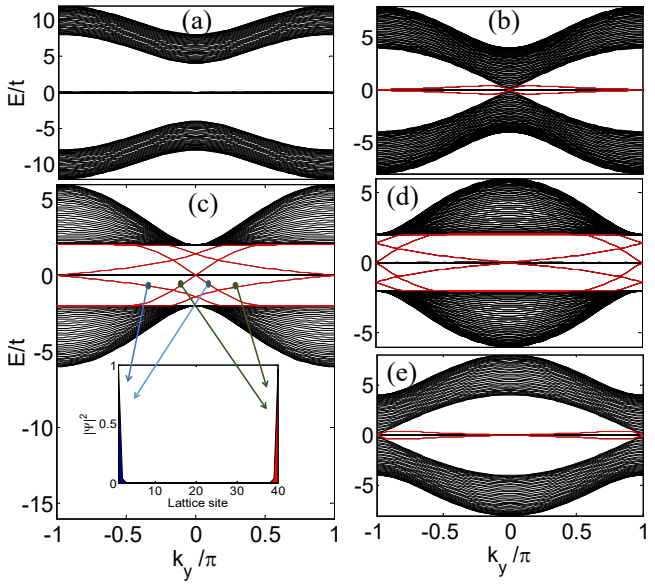

FIG. 3: (color online). Energy spectra and edge states. (a) $M = 4$; (b) $M = 2$; (c) $M = 1$; (d) $M = -1$; and (e) $M = -2$. The inse in (c) shows the density distributions of four typical edge modes. The edge modes in (a-e) are plotted in red. The lattice sites $L_x = 40$ under open boundary condition.

Without loss of generality, we consider the topological insulating state for $M = 1$ and further explore the properties of the edge modes in the first band gap. We find the correspondence between the helicity of these edge states and the polarization of photons, and thus named them as the Maxwell edge modes in this so-called topological Maxwell insulator. In particular, we reveal that this system exhibits an analogous quantum anomalous Hall effect [26], with the edge modes being strong spin-momentum locking as eigenstates of the spin operator $\hat{S}_y$. This means that the two bunches of quasiparticle streams on the two edges can be treated as the streams of polarized Maxwell quasiparticles moving along the y axis.

In Fig. 4(a), we numerically calculate the expectation value $\langle\hat{S}_y\rangle$ with the wave functions of the 2D lattice with $L_x = 100$. The results show that the distribution of $\langle\hat{S}_y(k_y, x)\rangle$ has two peaks localized at both of the left and right edges with opposite signs. To be more clearly, we

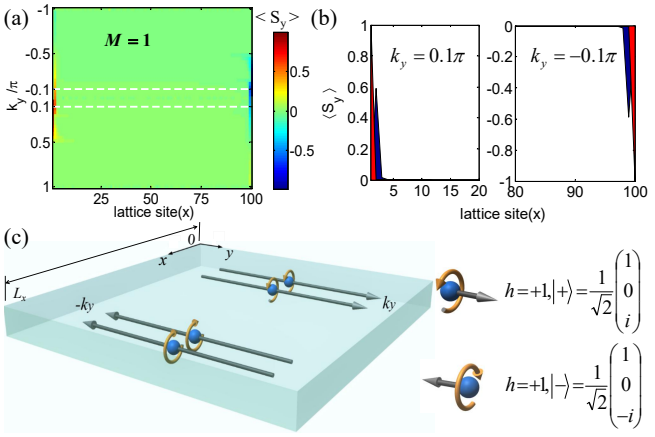

FIG. 4: (color online). Maxwell quasiparticles as the edge states in the 2D topological Maxwell insulators. (a) Expectation value of $\hat{S}_y$ as a function of k_y and x for the reduced 1D chain with lattice sites $L_x = 100$ under open boundary condition; (b) Density distribution of $\hat{S}_y(x)$ for $k_y = 0.1\pi$ and $k_y = -0.1\pi$; (c) Schematic diagram for Maxwell edges states $|+\rangle$ and $|-\rangle$ in the Maxwell topological insulator with opposite momenta, both corresponding to the right circularly-polarized photons with the helicity $h = +1$.

plot $\langle \hat{S}_y(x) \rangle$ for $k_y = 0.1\pi$ and $k_y = -0.1\pi$ in Fig. 4(b), respectively. It indicates that just the two edge states for each edge are the eigenstates of $\hat{S}_y$. The edge states on the $x = 0$ edge with positive eigenvalue are $|+\rangle = \frac{1}{\sqrt{2}}(1, 0, i)^T = \frac{1}{\sqrt{2}}(\mathbf{e}_x + i\mathbf{e}_z)^T$, and the ones on the $x = L_x$ edge with negative eigenvalue are $|-\rangle = \frac{1}{\sqrt{2}}(1, 0, -i)^T = \frac{1}{\sqrt{2}}(\mathbf{e}_x - i\mathbf{e}_z)^T$, where $\mathbf{e}_j$ $(j = x, y, z)$ are the unit vectors of Cartesian coordinates. Thus, the effective Hamiltonian of edge states is given by

$$H_{\text{edge}} = v_y k_y \hat{S}_y. \tag{7}$$

This effective Hamiltonian is nothing but the one-dimensioanl Maxwell Hamiltonian of circularly-polarized quasiparticles. The helicity operator is given by $\hat{h} = \hat{\mathbf{S}} \cdot \frac{\mathbf{k}}{|\mathbf{k}|} = \text{sign}(k_y)\hat{S}_y$, that is, the projection of the spin along the direction of the linear momentum [10, 27], where $\mathbf{k} = k_y \mathbf{e}_y$ denotes the momentum of Maxwell particles moving along the y direction. Thus, the edge quasiparticle-streams in this Maxwell topological insulator can be treated as Maxwell quasiparticle-streams with the same helicity $h \equiv \langle \hat{h} \rangle = +1$ for opposite momenta, which satisfies the helicity conservation of massless photons in quantum field theory, as shown in Fig. 4(c). In addition, the momentum $\mathbf{k}$ can also be considered as the wave vector of the plane electromagnetic wave propagated along the y axis, both of the edge states $|+\rangle$ $(k_y > 0)$ and $|-\rangle$ $(k_y < 0)$ with same helicity can be regarded as right circularly-polarized waves which consist of the two independent transverse polarization vectors $\mathbf{e}_x$ and $\mathbf{e}_z$ with opposite momenta. We can see from Fig. 4(c) that the Maxwell edge modes moving along $+y$ $(-y)$ direction correspond to the right circularly-polarized waves rotating anticlockwise (clockwise) in the xz plane (if one looks along the $-y$ axis) propagated along $+y$ $(-y)$ direction. Likewise, for the case $-2 < M < 0$ with the Chern number $\mathcal{C} = -2$, the Maxwell-edge modes on the $x = 0$ $(x = L_x)$ edge with $h = -1$ are corresponding to the left circularly-polarized waves propagated along $-y$ $(+y)$ direction similar to the schematic diagram in Fig. 4(c). Because the electromagnetic waves are transverse waves, there is no longitudinal component and thus no edge mode with the helicity $h = 0$, which corresponds to the unit wave vector of plane waves. So, the Maxwell edge modes here with such strong spin-momentum locking perfectly correspond to the circularly-polarized photons.

Discussions and conclusion.— We now address some possible concerns on the realistic cold-atom experiments. In our proposed OL scheme for implementing the model Hamiltonian (S.13), the major difficulty is to realize the spin-flip hopping terms along each direction, which will involves a number of Raman beams [19]. However, all of the lasers can be drawn from the same one with the small relative frequency shift induced by an acoustic optical modulator. The Maxwell points in the band structures with the related topological phase transition can be detected from the Bragg spectroscopy or Bloch-Zener oscillations, similar to the methods for detecting Dirac point in OLs [11, 12]. In addition, the Berry curvature and thus the Chern numbers (Berry phases) can be measured by the newly-developed technique of tomography of Bloch band in OLs [28, 29], and the Chern numbers can also be revealed from the shift of the hybrid Wannier center of an atomic cloud [19, 30–32].

In summary, we have explored the topological properties of Maxwell quasiparticles emerged in Maxwell metals and Maxwell insulators. The proposed model could be realized in OLs and the exotic properties of these topological quasiparticles can be detected in cold-atom experiments. Moreover, the properties of the topological Maxwell quasiparticles analogous to the Dirac and Weyl fermions can be further investigated, such as wave dynamics of the Maxwell fermions by studying the relativistic Zitterbewegung oscillations [33, 34] or Klein tunneling [35] in the Maxwell insulators, the transport properties of the Maxwell fermions and so forth.

We thank Hai-Jun Zhang and Rui-Bin Liu for useful discussions. This work was supported by the NKRDP of China (Grant No. 2016YFA0301803), the NSFC (Grants No. 11474153 and 11604103), and the PCSIRT (Grant No. IRT1243). D.-W. Z. was also supported by the NSF of Guangdong Province (Grant No. 2016A030313436) and the Startup Foundation of SCNU.

* Electronic address: zdanwei@126.com
† Electronic address: slzhu@nju.edu.cn

[1] F. Wilczek, Why Are There Analogies Between Condensed Matter and Particle Theory? Phys. Today **51**, 11 (1998).
[2] A. H. Castro Neto, F. Guinea, N. M. R. Peres, K. S. Novoselov, and A. K. Geim, The electronic properties of graphene, Rev. Mod. Phys. **81**, 109162 (2009).
[3] X. Wan, A. M. Turner, A. Vishwannath, and S. Y. Savrasov, Topological semimetal and Fermi-arc surface states in the electronic structure of pyrochlore iridates, Phys. Rev. B **83**, 205101 (2011).
[4] S.-Y. Xu, I. Belopolski, N. Alidoust, M. Neupane, G. Bian, C. Zhang, R. Sankar, G. Chang, Z. Yuan, C. C. Lee, S.-M. Huang, H. Zheng, J. Ma, D. S. Sanchez, B. Wang, A. Bansil, F. Chou, P. P. Shibayev, H. Lin, S. Jia, and M. Z. Hasan, Discovery of a Weyl fermion semimetal and topological Fermi arcs, Science **349**, 613 (2015).
[5] B.-Q. Lv, H.-M. Weng, B.-B. Fu, X.-P. Wang, H. Miao, J. Ma, P. Richard, X.-C. Huang, L.-X. Zhao, G.-F. Chen, Z. Fang, X. Dai, T. Qian, and H. Ding, Experimental Discovery of Weyl Semimetal TaAs, Phys. Rev. X **5**, 031013 (2015).
[6] L. Lu, L. Fu, J. D. Joannopoulos, and M. Soljačić, Weyl points and line nodes in gyroid photonic crystals, Nat. Photonics **7**, 294 (2013).
[7] M. Z. Hasan and C. L. Kane, Topological insulators, Rev. Mod. Phys. **82**, 3045 (2010).
[8] X.-L. Qi and S.-C. Zhang, Topological insulators and superconductors, Rev. Mod. Phys. **83**, 1057 (2011).
[9] B. Bradlyn, J. Cano, Z. Wang, M. G. Vergniory, C. Felser, R. J. Cava, and B. A. Bernevig, Beyond Dirac and Weyl fermions: Unconventional quasiparticles in conventional crystals, Science **353**, 5037 (2016).
[10] Z. Lan, N. Goldman, A. Bermudez, W. Lu, and P. Öhberg, Dirac-Weyl fermions with arbitrary spin in two-dimensional optical superlattices, Phys. Rev. B **84**, 165115 (2011).
[11] S.-L. Zhu, B.-G. Wang, and L.-M. Duan, Simulation and Detection of Dirac Fermions with Cold Atoms in an Optical Lattice, Phys. Rev. Lett. **98**, 260402 (2007).
[12] L. Tarruell, D. Greif, T. Uehlinger, G. Jotzu, and T. Esslinger, Creating, moving and merging Dirac points with a Fermi gas in a tunable honeycomb lattice, Nature (London) **483**, 302 (2012).
[13] L. Duca, T. Li, M. Reitter, I. Bloch, M. Schleier-Smith, and T. Schneider, An Aharonov-Bohm interferometer for determining Bloch band topology, Science **347**, 288 (2015).
[14] T. Dubcek, C .J. Kennedy, L. Lu, W. Ketterle, M. Soljacic, and H. Buljan, Weyl Points in Three-Dimensional Optical Lattices: Synthetic Magnetic Monopoles in Momentum Space, Phys. Rev. Lett. **114**, 225301 (2015).
[15] D.-W. Zhang, Z. D. Wang, and S.-L. Zhu, Relativistic quantum effects of Dirac particles simulated by ultracold atoms, Front. Phys. **7**, 31 (2012).
[16] D.-W. Zhang, S.-L. Zhu, and Z. D. Wang, Simulating and exploring Weyl semimetal physics with cold atoms in a two-dimensional optical lattice, Phys. Rev. A **92**, 013632 (2015).
[17] R. Oppenheimer, Note on Light Quanta and the Electromagnetic Field, Phys. Rev. **38**, 725 (1931).
[18] R. Good and T. Nelson, *Classical Theory of Electric and Magnetic Fields* (Academic Press, New York, 1971).
[19] See the supplemental materials for more details on the derivation of the Maxwell equations in the form of the Schrödinger equation, the schemes to realize the Maxwell Hamiltonian with cold atoms in 2D optical lattices, the derivation of the topological invariants, and a scheme to measure the topological Chern numbers with cold atoms.
[20] D. Jaksch and P. Zoller, Creation of effective magnetic fields in optical lattices: the Hofstadter butterfly forcold neutral atoms, New J. Phys. **5**, 56 (2003).
[21] J. Dalibard, F. Gerbier, G. Juzeliūnas, and P. Öhberg, Artificial gauge potentials for neutral atoms, Rev. Mod. Phys. **83**, 1523 (2011).
[22] N. Goldman, G. Juzeliūnas, P. Öhberg, and I. B. Spielman, Light-induced gauge fields for ultracold atoms, Rep. Prog. Phys. **77**, 126401 (2014).
[23] H. Miyake, G. A. Siviloglou, C. J. Kennedy, W. C. Burton, and W. Ketterle, Realizing the Harper Hamiltonian with Laser-Assisted Tunneling in Optical Lattices, Phys. Rev. Lett. **111**, 185302 (2013);
[24] S.-T. Wang, D.-L. Deng, and L.-M. Duan, Probe of Three-Dimensional Chiral Topological Insulators in an Optical Lattice, Phys. Rev. Lett. **113**, 033002 (2014).
[25] Y. He, J. Moore and C. M. Varma, Berry phase and anomalous Hall effect in a three-orbital tight-binding Hamiltonian, Phys. Rev. B **85**, 155106 (2012).
[26] N. Nagaosa, J. Sinova, S. Onoda, A. H. MacDonald, and N. P. Ong, Anomalous Hall effect, Rev. Mod. Phys. **82**, 1539 (2010).
[27] W. Greiner, *Relativistic Quantum Mechanic: Wave Equations* (Springer, Berlin, 2000).
[28] N. Fläschner, B. S. Rem, M. Tarnowski, D. Vogel, D. S. Lühmann, K. Sengstock, C. Weitenberg, Experimental Reconstruction of the Berry Curvature in a Floquet Bloch Band, Science **352**, 1901 (2016).
[29] T. Li, L. Duca, M. Reitter, F. Grusdt, E. Demler, M. Endres, M. Schleier-Smith, I. Bloch, and U. Schneider, Bloch state tomography using Wilson lines, Science **352**, 1904 (2016).
[30] M. Lohse, C. Schweizer, O. Zilberberg, M. Aidelsburger, and I. Bloch, A Thouless quantum pump with ultracold bosonic atoms in an optical superlattice, Nature Phys. **12**, 350 (2016).
[31] H.-I. Lu, M. Schemmer, L. M. Aycock, D. Genkina, S. Sugawa, and I. B. Spielman, Geometrical Pumping with a Bose-Einstein Condensate, Phys. Rev. Lett. **116**, 200402 (2016).
[32] S. Nakajima, T. Tomita, S. Taie, T. Ichinose, H. Ozawa, L. Wang, M. Troyer, and Y. Takahashi, Topological Thouless pumping of ultracold fermions, Nature Phys. **12**, 296 (2016).
[33] J. Y. Vaishnav and C. W. Clark, Observing Zitterbewegung with Ultracold Atoms, Phys. Rev. Lett. **100**, 153002 (2008).
[34] Z. Li, H.-Q. Wang, D.-W. Zhang, S.-L. Zhu, and D.-Y. Xing, Dynamics of Weyl quasiparticles in an optical lattice, Phys. Rev. A **94**, 043617 (2016).
[35] D.-W. Zhang, Z.-Y. Xue, H. Yan, Z. D. Wang, and S.-L. Zhu, Macroscopic Klein tunneling in spin-orbit-coupled Bose-Einstein condensates, Phys. Rev. A **85**, 013628 (2012).

SUPPLEMENTAL MATERIAL: MAXWELL QUASIPARTICLES EMERGED IN OPTICAL LATTICES

In this supplemental materials, we provide more details on the derivation of the Maxwell equations in the form of the Schrödinger equation, the schemes to realize the Maxwell Hamiltonian with cold atoms in 2D optical lattices, the derivation of the topological invariants, and a scheme to measure the topological Chern numbers with cold atoms.

MAXWELL EQUATIONS IN THE FORM OF THE SCHRÖDINGER EQUATION

The well-known Maxwell equations in a vacuum are given by

$$\begin{aligned} \frac{1}{c}\frac{\partial \tilde{\mathbf{E}}}{\partial t} &= \nabla \times \tilde{\mathbf{H}}, \qquad \nabla \cdot \tilde{\mathbf{E}} = 0, \\ -\frac{1}{c}\frac{\partial \tilde{\mathbf{H}}}{\partial t} &= \nabla \times \tilde{\mathbf{E}}, \qquad \nabla \cdot \tilde{\mathbf{H}} = 0, \end{aligned} \tag{S.1}$$

where $\tilde{\mathbf{E}} = \sqrt{\varepsilon_0}\mathbf{E}$ with $\mathbf{E}$ being the electric field, $\tilde{\mathbf{H}} = \sqrt{\mu_0}\mathbf{H}$ with $\mathbf{H}$ being the magnetizing field, $c = 1/\sqrt{\varepsilon_0\mu_0}$ is the speed of light in the vacuum, and ε_0, μ_0 are the permeability and permittivity of the vacuum, respectively. If we define the photon wave function as $\mathbf{\Phi}(\mathbf{r},t) = \tilde{\mathbf{E}}(\mathbf{r},t) + i\tilde{\mathbf{H}}(\mathbf{r},t)$ [1, 2] , we have $\nabla\cdot\mathbf{\Phi} = 0$ and $\nabla\times\mathbf{\Phi} = \nabla\times\tilde{\mathbf{E}} + i\nabla\times\tilde{\mathbf{H}} = \frac{i}{c}\frac{\partial \mathbf{\Phi}}{\partial t}$. Thus we can obtain

$$\varepsilon_{\alpha\beta\gamma}\frac{\partial \Phi_m^\gamma}{\partial \beta} = \frac{i}{c}\frac{\partial \Phi_m^\alpha}{\partial t} \Rightarrow ci\varepsilon_{\alpha\beta\gamma}\hat{P}_\beta \Phi_m^{\ \gamma} = i\hbar\frac{\partial \Phi_m^\alpha}{\partial t}, \tag{S.2}$$

where $\hat{P}_\beta = -i\hbar\partial_\beta$. Let $\hat{S}^\beta_{\alpha\gamma} = i\varepsilon_{\alpha\beta\gamma}$ with $\varepsilon_{\alpha\beta\gamma}$ $(\alpha,\beta,\gamma = x,y,z)$ being the Levi-Civita symbol. We can rewrite the Maxwell Eqs (S.1) as

$$i\hbar\frac{\partial}{\partial t}\mathbf{\Phi} = c\hat{\mathbf{S}}\cdot\hat{\mathbf{P}}\mathbf{\Phi}, \tag{S.3}$$

where the spin matrices are defined as

$$\begin{aligned} \hat{S}_x = \hat{S}^1 &= i\begin{pmatrix} \varepsilon_{111} & \varepsilon_{112} & \varepsilon_{113} \\ \varepsilon_{211} & \varepsilon_{212} & \varepsilon_{213} \\ \varepsilon_{311} & \varepsilon_{312} & \varepsilon_{313} \end{pmatrix} = \begin{pmatrix} 0 & 0 & 0 \\ 0 & 0 & -i \\ 0 & i & 0 \end{pmatrix}, \\ \hat{S}_y = \hat{S}^2 &= i\begin{pmatrix} \varepsilon_{121} & \varepsilon_{122} & \varepsilon_{123} \\ \varepsilon_{221} & \varepsilon_{222} & \varepsilon_{223} \\ \varepsilon_{321} & \varepsilon_{322} & \varepsilon_{323} \end{pmatrix} = \begin{pmatrix} 0 & 0 & i \\ 0 & 0 & 0 \\ -i & 0 & 0 \end{pmatrix}, \\ \hat{S}_z = \hat{S}^3 &= i\begin{pmatrix} \varepsilon_{131} & \varepsilon_{132} & \varepsilon_{133} \\ \varepsilon_{231} & \varepsilon_{232} & \varepsilon_{233} \\ \varepsilon_{331} & \varepsilon_{332} & \varepsilon_{333} \end{pmatrix} = \begin{pmatrix} 0 & -i & 0 \\ i & 0 & 0 \\ 0 & 0 & 0 \end{pmatrix}. \end{aligned} \tag{S.4}$$

One can check that $[\hat{S}_x, \hat{S}_y] = i\hat{S}_z$, $\hat{\mathbf{S}}\times\hat{\mathbf{S}} = i\hat{\mathbf{S}}$, $S^2 = S_x^2 + S_y^2 + S_z^2 = 2\begin{pmatrix} 1 & 0 & 0 \\ 0 & 1 & 0 \\ 0 & 0 & 1 \end{pmatrix} = S(S+1)$, and $S = 1$. Thus we obtain the Maxwell equations in the form of the Schrödinger equation, and the related Hamiltonian of single photon with spin-1 is $\hat{H} = c\hat{\mathbf{S}}\cdot\hat{\mathbf{P}}$. We can easily obtain the eigenstates of $\hat{S}_y$, which are given by $\hat{S}_y\Phi = s_y\Phi$ and

$$\begin{aligned} \Phi_1 &= \frac{1}{\sqrt{2}}\begin{pmatrix} 1 \\ 0 \\ i \end{pmatrix}; \quad s_y = 1 \\ \Phi_0 &= \begin{pmatrix} 0 \\ 1 \\ 0 \end{pmatrix}; \quad s_y = 0 \\ \Phi_{-1} &= \frac{1}{\sqrt{2}}\begin{pmatrix} 1 \\ 0 \\ -i \end{pmatrix}; \quad s_y = -1 \end{aligned} \tag{S.5}$$

The above derivation can be generalized to an anisotropic medium. In a region without free charges and currents, the Maxwell equations are given by

$$\begin{aligned} \nabla \times \mathbf{E} &= -\frac{\partial \mathbf{B}}{\partial t}, \quad \nabla \cdot \mathbf{E} = 0, \\ \nabla \times \mathbf{H} &= \frac{\partial \mathbf{D}}{\partial t}, \quad \nabla \cdot \mathbf{B} = 0, \end{aligned} \tag{S.6}$$

where the displacement field $\mathbf{D} = \varepsilon_0 \varepsilon_r \mathbf{E}$, the magnetic field $\mathbf{B} = \mu_0 \mu_r \mathbf{H}$, ε_r and μ_r are the relative permittivity and permeability, respectively. In the anisotropic medium, ε_r and μ_r become tensors rather than numbers. To simplify the proceeding analysis, we assume that the tensors ε_r and μ_r are simultaneously diagonalized, i.e.,

$$\varepsilon_r = \begin{pmatrix} \varepsilon_x & 0 & 0 \\ 0 & \varepsilon_y & 0 \\ 0 & 0 & \varepsilon_z \end{pmatrix}, \ \mu_r = \begin{pmatrix} \mu_x & 0 & 0 \\ 0 & \mu_y & 0 \\ 0 & 0 & \mu_z \end{pmatrix}. \tag{S.7}$$

The relationships between $\mathbf{D}$ and $\mathbf{E}$, $\mathbf{B}$ and $\mathbf{H}$ now become

$$\begin{pmatrix} D_x \\ D_y \\ D_z \end{pmatrix} = \varepsilon_0 \begin{pmatrix} \varepsilon_x & 0 & 0 \\ 0 & \varepsilon_y & 0 \\ 0 & 0 & \varepsilon_z \end{pmatrix} \begin{pmatrix} E_x \\ E_y \\ E_z \end{pmatrix}, \ \begin{pmatrix} B_x \\ B_y \\ B_z \end{pmatrix} = \mu_0 \begin{pmatrix} \mu_x & 0 & 0 \\ 0 & \mu_y & 0 \\ 0 & 0 & \mu_z \end{pmatrix} \begin{pmatrix} H_x \\ H_y \\ H_z \end{pmatrix}. \tag{S.8}$$

Thus Eq. (S.6) can be rewritten as

$$\begin{aligned} \nabla \times \mathbf{E} = -\frac{\partial \mathbf{B}}{\partial t} &\Rightarrow \epsilon_{\alpha\beta\gamma} \frac{\partial E_\gamma}{\partial \beta} = -\frac{\partial B_\alpha}{\partial t} \Rightarrow \frac{c}{\sqrt{\varepsilon_\gamma \mu_\alpha}} \epsilon_{\alpha\beta\gamma} \frac{\partial \tilde{E}_\gamma}{\partial \beta} = -\frac{\partial \tilde{H}_\alpha}{\partial t}, \\ \nabla \times \mathbf{H} = \frac{\partial \mathbf{D}}{\partial t} &\Rightarrow \epsilon_{\alpha\beta\gamma} \frac{\partial H_\gamma}{\partial \beta} = \frac{\partial D_\alpha}{\partial t} \Rightarrow \frac{c}{\sqrt{\varepsilon_\alpha \mu_\gamma}} \epsilon_{\alpha\beta\gamma} \frac{\partial \tilde{H}_\gamma}{\partial \beta} = \frac{\partial \tilde{E}_\alpha}{\partial t}, \end{aligned} \tag{S.9}$$

where $\tilde{E}_\alpha = \sqrt{\varepsilon_0 \varepsilon_\alpha} E_\alpha$, $\tilde{H}_\alpha = \sqrt{\mu_0 \mu_\alpha} H_\alpha$. Then we define the photon wave function as $\mathbf{\Phi}(\mathbf{r}, t) = \tilde{\mathbf{E}}(\mathbf{r}, t) + i\tilde{\mathbf{H}}(\mathbf{r}, t)$, we have $\nabla \cdot \mathbf{\Phi} = 0$, and

$$i\hbar \frac{\partial \Phi_m^\alpha}{\partial t} = \frac{c}{\sqrt{\varepsilon_\gamma \mu_\alpha}} (i\epsilon_{\alpha\beta\gamma}) \frac{\hbar}{i} \frac{\partial \tilde{E}_\gamma}{\partial \beta} + i \frac{c}{\sqrt{\varepsilon_\alpha \mu_\gamma}} (i\epsilon_{\alpha\beta\gamma}) \frac{\hbar}{i} \frac{\partial \tilde{H}_\gamma}{\partial \beta}. \tag{S.10}$$

Let $\nu_{\alpha\gamma} = c/\sqrt{\varepsilon_\alpha \mu_\gamma}$, $\nu_{\gamma\alpha} = c/\sqrt{\varepsilon_\gamma \mu_\alpha}$, $\hat{P}_\beta = -i\hbar\partial_\beta$, when $\varepsilon_\alpha \mu_\gamma = \varepsilon_\gamma \mu_\alpha$, that is, $\nu_{\alpha\gamma} = \nu_{\gamma\alpha}$ [the condition for obtaining a hermitian Hamiltonian, see Eq. (S.12)], then we can further rewrite Eq. (S.10) as

$$i\hbar \frac{\partial \Phi_m^\alpha}{\partial t} = \nu_{\alpha\gamma} (i\epsilon_{\alpha\beta\gamma}) \hat{P}_\beta \frac{\partial \Phi_m^\gamma}{\partial \beta}. \tag{S.11}$$

Thus we obtain the following Schrödinger's equation

$$i\hbar \frac{\partial}{\partial t} \begin{pmatrix} \Phi_m^x \\ \Phi_m^y \\ \Phi_m^z \end{pmatrix} = \begin{pmatrix} 0 & -i\nu_{xy}\hat{P}_z & i\nu_{xz}\hat{P}_y \\ i\nu_{yx}\hat{P}_z & 0 & -i\nu_{yz}\hat{P}_x \\ -i\nu_{zx}\hat{P}_y & i\nu_{zy}\hat{P}_x & 0 \end{pmatrix} \begin{pmatrix} \Phi_m^x \\ \Phi_m^y \\ \Phi_m^z \end{pmatrix}. \tag{S.12}$$

This corresponds to the Maxwell equations in the anisotropic medium in the Schrödinger's form

$$i\hbar \frac{\partial}{\partial t} \mathbf{\Phi} = \hat{H} \mathbf{\Phi},$$

where the Hamiltonian is given by

$$\hat{H} = v_x \hat{S}_x \hat{P}_x + v_y \hat{S}_y \hat{P}_y + v_z \hat{S}_z \hat{P}_z.$$

Here $\hat{S}_\beta = (\hat{S}_{\alpha\gamma})^\beta = i\epsilon_{\alpha\beta\gamma}$ has the same form as that in Eq. (S.4). Noted that, $v_x = \nu_{yz} = \nu_{zy}$, $v_y = \nu_{zx} = \nu_{xz}$, and $v_z = \nu_{xy} = \nu_{yx}$ are the necessary and sufficient condition to obtain a hermitian Hamiltonian in Eq. (S12). It returns to the free space situation in Eq. (S.3) when $\varepsilon_r = \mu_r = 1$.

REALIZING THE 2D MODEL HAMILTONIAN IN OPTICAL LATTICES

In this section, we propose two different schemes to realize the Maxwell quasi-particles in the 2D optical lattices.

In the first part, we provide some details on the realization scheme based on the Raman-assisted tunneling method [3–5] to implement the following 2D model Hamiltonian of Maxwell insulators and Maxwell metals:

$$\begin{aligned}\hat{H}_{2D} =& t\sum_{\mathbf{r}}\left[\hat{H}_{\mathbf{rx}}+\hat{H}_{\mathbf{ry}}+\left(\Gamma_0\hat{a}^{\dagger}_{\mathbf{r},0}\hat{a}_{\mathbf{r},\uparrow}+\text{H.c.}\right)\right],\\ \hat{H}_{\mathbf{rx}} =& -\hat{a}^{\dagger}_{\mathbf{r}-\mathbf{x},0}(\hat{a}_{\mathbf{r},\downarrow}+i\hat{a}_{\mathbf{r},\uparrow})+\hat{a}^{\dagger}_{\mathbf{r}+\mathbf{x},0}(\hat{a}_{\mathbf{r},\downarrow}-i\hat{a}_{\mathbf{r},\uparrow})+\text{H.c.},\\ \hat{H}_{\mathbf{ry}} =& \hat{a}^{\dagger}_{\mathbf{r}-\mathbf{y},\uparrow}(\hat{a}_{\mathbf{r},\downarrow}+i\hat{a}_{\mathbf{r},0})-\hat{a}^{\dagger}_{\mathbf{r}+\mathbf{y},\uparrow}(\hat{a}_{\mathbf{r},\downarrow}-i\hat{a}_{\mathbf{r},0})+\text{H.c.}.\end{aligned} \tag{S.13}$$

We can use noninteracting fermionic (or bosonic) atoms in a titled square optical lattice and choose three atomic

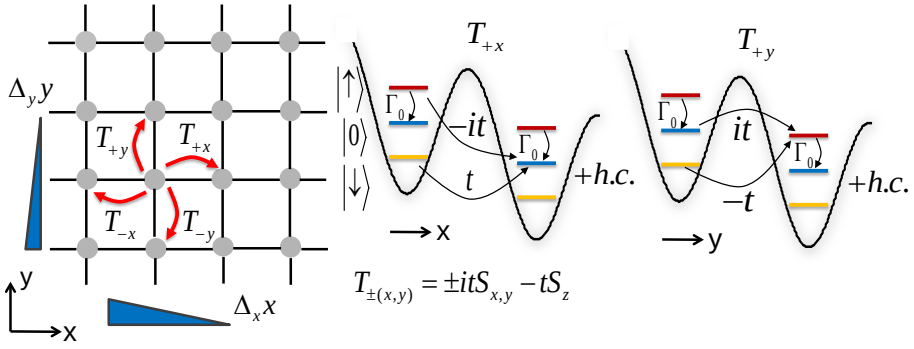

FIG. S5: (Color online) Schematic diagram of realizing the model Hamiltonian (S.13) with the spin-flip hopping and on-site spin-flip terms with cold fermionic atoms in a tilted square optical lattice. The three atomic internal states $|\uparrow\rangle, |0\rangle, |\downarrow\rangle$ form the (pseudo)spin-1 basis and the required atomic spin-flip hopping, such as T_{+x} and T_{+y}, are shown in the figure. Along the x (y) axis, the natural hopping is suppressed due to a large tilt potential $\Delta_x x$ ($\Delta_y y$) with the energy difference Δ_x (Δ_y) per lattice site. The required hopping can then be restored and engineered by using proper Raman lasers.

internal states in the ground state manifold to encode the three spin states $|s\rangle$ ($s = \uparrow, 0, \downarrow$), as shown in Fig. S5. The other levels in the ground state manifold are irrelevant because they can be depopulated by the optical pumping and transition. Here, the on-site spin-flip term $\Gamma_0\hat{a}^{\dagger}_{\mathbf{r},0}\hat{a}_{\mathbf{r},\uparrow}$ can be easily achieved by applying a simple radio-frequency field or Raman beams for coupling the atomic internal states. Thus, the major difficulty for implementing this model Hamiltonian is to realize the spin-flip hopping terms $\hat{H}_{\mathbf{rx}}$ and $\hat{H}_{\mathbf{ry}}$ along each direction shown in Fig. S5. Here the spin-flip hopping terms can be diagrammatically visualized as

$$\begin{aligned}&x\text{-direction: } T_{+x}+T_{-x} = \overset{\times}{\curvearrowleft}|1_x\rangle\overset{\sqrt{2}}{\curvearrowright}|0\rangle+|0\rangle\overset{-\sqrt{2}}{\curvearrowleft}|2_x\rangle\overset{\times}{\curvearrowright}+\text{H.c.},\\ &y\text{-direction: } T_{+y}+T_{-y} = \overset{\times}{\curvearrowleft}|1_y\rangle\overset{-\sqrt{2}}{\curvearrowright}|\uparrow\rangle+|\uparrow\rangle\overset{\sqrt{2}}{\curvearrowleft}|2_y\rangle\overset{\times}{\curvearrowright}+\text{H.c.},\end{aligned}$$

where $\overset{\times}{\curvearrowright}$ indicates that the hopping is forbidden along this direction, and the states $|1_x\rangle = (|\downarrow\rangle - i|\uparrow\rangle)/\sqrt{2}$, $|2_x\rangle = (|\downarrow\rangle + i|\uparrow\rangle)/\sqrt{2}$, $|1_y\rangle = (|\downarrow\rangle - i|0\rangle)/\sqrt{2}$, $|2_y\rangle = (|\downarrow\rangle + i|0\rangle)/\sqrt{2}$ are superpositions of the original spin-basis vectors $|\uparrow\rangle$, $|0\rangle$, $|\downarrow\rangle$.

We can use Raman-assisted tunneling [3–5] to realize the spin-flip hopping terms depicted above. First, the required broken parity (left-right) symmetry in these hopping terms can be achieved by titling the square optical lattice with a homogeneous energy gradient along the x and y-directions. This can be realized through the natural gravitational field or the gradient of a dc- or ac-Stark shift. Note that the Raman-assisted hopping in tilted optical lattices has been demonstrated in recent experiments [4]. In our scheme, we require different linear energy shifts per site $\Delta_{x,y}$ along the x and y-directions as shown in Fig. S5, such as $\Delta_x \approx 1.5\Delta_y$. Secondly, the natural hopping is suppressed by the large tilt potential $\Delta_y \gg t_0$ with t_0 denoting the natural tunneling rate. Under this condition, the hopping probability $(t_0/\Delta_y)^2$ induced by the natural tunneling is negligible in this tilted lattice. Finally, the hopping terms can be restored and engineered by application of two-photon Raman transitions with the laser beams of proper configurations.

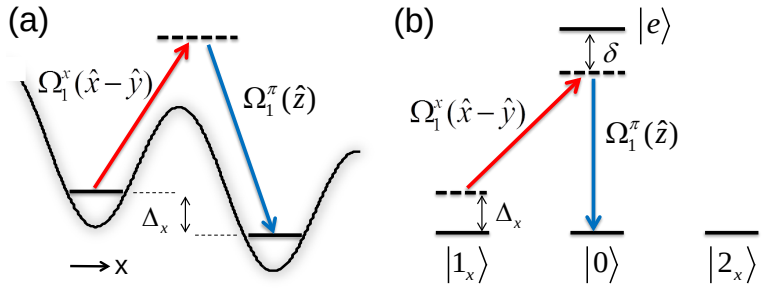

FIG. S6: (Color online) (a) A linear tilt Δ_x per lattice site along x-direction and the Raman beams Ω_1^x and Ω_1^π for addressing atoms. (b) The two Raman beams used to induce the required atomic tunneling term $T_{+x}^{(1)}$. The vector units in brackets show the polarization direction of the corresponding beam.

Let us first consider a single term $T_{+x}^{(1)} = \hat{a}^\dagger_{\mathbf{r}+\mathbf{x},0}(\hat{a}_{\mathbf{r},\downarrow} - i\hat{a}_{\mathbf{r},\uparrow})$ to explain our Raman-assisted hopping scheme. This corresponds to an atom in the spin state $|1_x\rangle = (|\downarrow\rangle - i|\uparrow\rangle)/\sqrt{2}$ at site $\mathbf{r}$ hopping to site $\mathbf{r}+\mathbf{x}$ while changing the spin state to $|0\rangle$ with hopping strength $\sqrt{2}$, which can be diagrammatically visualized as

$$T_{+x}^{(1)} = \hat{a}^\dagger_{\mathbf{r}+\mathbf{x},0}(\hat{a}_{\mathbf{r},\downarrow} - i\hat{a}_{\mathbf{r},\uparrow}) \qquad \Longleftrightarrow \qquad x\text{-direction:} \quad \overset{\times}{\curvearrowleft}|1_x\rangle \overset{\sqrt{2}}{\curvearrowright}|0\rangle.$$

This hopping term can be achieved by two Raman beams $\Omega_1^x(\hat{x}-\hat{y}) = \sqrt{2}\Omega_0 e^{ikz}$ polarized along $(\hat{x}-\hat{y})$-direction and $\Omega_1^\pi(\hat{z}) = \Omega_0 e^{ikx}$ with π-polarization along $\hat{z}$-direction, as shown in Fig. S6. Here the population of the excited state $|e\rangle$ which is estimated by $|\Omega_0/\delta|^2$ is negligible due to the large single-photon detuning δ. The two-photon detuning Δ_x matching the linear energy shift of the lattice per site ensures that it only allows $|1_x\rangle$ hopping to the right, and the other direction is forbidden by a large energy mismatch $2\Delta_x$. We can address the spin states through the polarization selection rule since the original spin basis $|\downarrow\rangle, |0\rangle, |\uparrow\rangle$ differ in the magnetic quantum number by one successively. Thus, a π-polarized beam Ω_1^π excites the state $|0\rangle$ and a linear $(\hat{x}-\hat{y})$-polarized beam Ω_1^x excites the superposition state $|1_x\rangle = (|\downarrow\rangle - i|\uparrow\rangle)/\sqrt{2}$ as the polarization $(\hat{x}-\hat{y}) \sim (\sigma^+ - i\sigma^-)$. These two beams together induce a Raman-assisted hopping between $|1_x\rangle$ and $|0\rangle$. The hopping amplitude and phase are controlled by the corresponding Raman beam amplitude and phase [3–5], which can be written as

$$t_{\mathbf{r},+\mathbf{x}} = \frac{\sqrt{2}|\Omega_0|^2}{\delta}\beta e^{i\delta\mathbf{k}\cdot\mathbf{r}}, \quad \beta = \int dx w^*(x+a)e^{-ikx}w(x)\int dy w^*(y)w(y). \tag{S.14}$$

Here $\delta\mathbf{k} = (-k, 0)$ for this hopping term and we have used factorization of the Wannier function $w(\mathbf{r}') = w(x')w(y')$ in a square lattice. If we adjust the interfering angle of the lattice beams to satisfy the condition $ka = 2\pi$, the site dependent phase term can always be reduced to $e^{i\delta\mathbf{k}\cdot\mathbf{r}} = 1$. Under this condition, we can obtain the required hopping strength $t_1 = \sqrt{2}t$ with $t = \beta|\Omega_0|^2/\delta$.

All the other hopping terms in the model Hamiltonian can be realized in a similar manner. For examples, the hopping term $T_{-x}^{(2)} = -\hat{a}^\dagger_{\mathbf{r}-\mathbf{x},0}(\hat{a}_{\mathbf{r},\downarrow} + i\hat{a}_{\mathbf{r},\uparrow})$ can be realized by the two Raman beams $\Omega_1^\pi(\hat{z}) = \Omega_0 e^{ikx}$ and $\Omega_2^x(\hat{x}+\hat{y}) = -\sqrt{2}\Omega_0 e^{ikz}$ polarized along $(\hat{x}+\hat{y})$-direction, which couple the state $|0\rangle$ and $|2_x\rangle = (|\downarrow\rangle + i|\uparrow\rangle)/\sqrt{2}$ since $(\hat{x}+\hat{y}) \sim (\sigma^+ + i\sigma^-)$. Thus, the hopping term along the x axis $\hat{H}_{\mathbf{rx}}$ can be realized by three Raman beams with the configuration shown in Fig. S7 (a). Along the y axis, the hopping term $T_{+y}^{(1)} = -\hat{a}^\dagger_{\mathbf{r}+\mathbf{y},\uparrow}(\hat{a}_{\mathbf{r},\downarrow} - i\hat{a}_{\mathbf{r},0})$ can be realized by three Raman beams $\Omega_1^y(\sigma^-) = \Omega_0 e^{iky}$ which excites the state $|\uparrow\rangle$, and $\Omega_2^y(\sigma^+) = -\sqrt{2}\Omega_0 e^{ikz}$ and $\Omega_2^\pi(\hat{z}) = i\sqrt{2}\Omega_0 e^{-iky}$ together excite effectively the state $|1_y\rangle = (|\downarrow\rangle - i|0\rangle)/\sqrt{2}$. Similarly, the hopping term $T_{-y}^{(2)} = \hat{a}^\dagger_{\mathbf{r}-\mathbf{y},\uparrow}(\hat{a}_{\mathbf{r},\downarrow} + i\hat{a}_{\mathbf{r},0})$ can be realized by two additional Raman beams $\Omega_3^y(\sigma^+) = \sqrt{2}\Omega_0 e^{ikz}$ and $\Omega_3^\pi(\hat{z}) = i\sqrt{2}\Omega_0 e^{-iky}$ which effectively excite the state $|2_y\rangle = (|\downarrow\rangle + i|0\rangle)/\sqrt{2}$. Note that here a wave-vector difference $\delta\mathbf{k} = (0, -2k)$ and a two-photon energy detuning Δ_y guarantee the hopping along y-direction. The laser configuration for realizing the desired hopping term along the y axis $\hat{H}_{\mathbf{ry}}$ is shown in Fig. S7 (b). With the eight laser beams required to realize the full Hamiltonian as shown in Fig. S7 (c), it is important to forbid the undesired tunneling terms. To this end, we require different linear energy shifts per site Δ_x and Δ_y along the x and y-directions, which can be achieved by adjusting the direction of the gradient field to be in different angles with respect to the axes of the optical lattice.

In the second part, we point out that the Maxwell points and the associated Maxwell quasiparticles may be alternatively realized by using single-component fermionic atoms in optical lattices with three sublattices, such as an

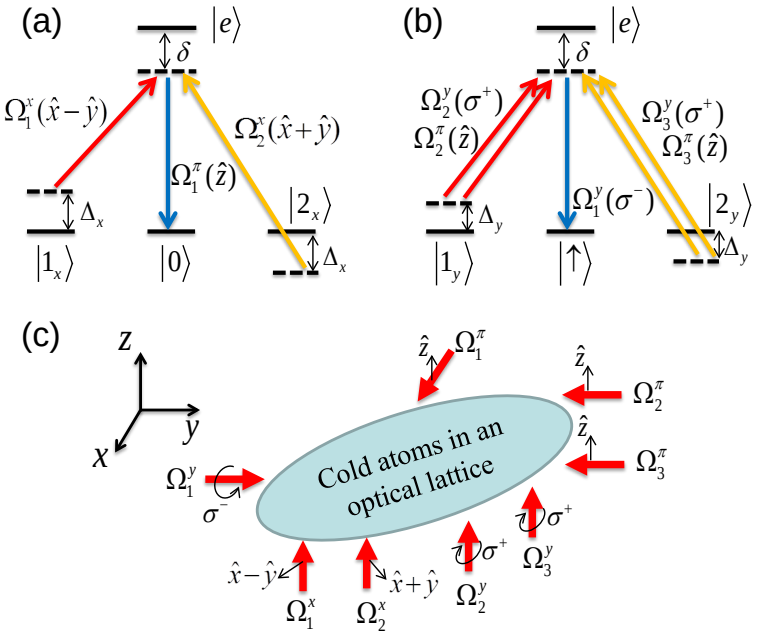

FIG. S7: (Color online) Schematics of the laser configuration to realize the Hamiltonian. (a) The three Raman beams for inducing the desired hopping along x axis; (b) The five Raman beams for inducing the desired hopping along y axis; (c) The total lasers with the corresponding polarization and propagation direction. The detuning in each direction matches the frequency offset of the corresponding Raman beams.

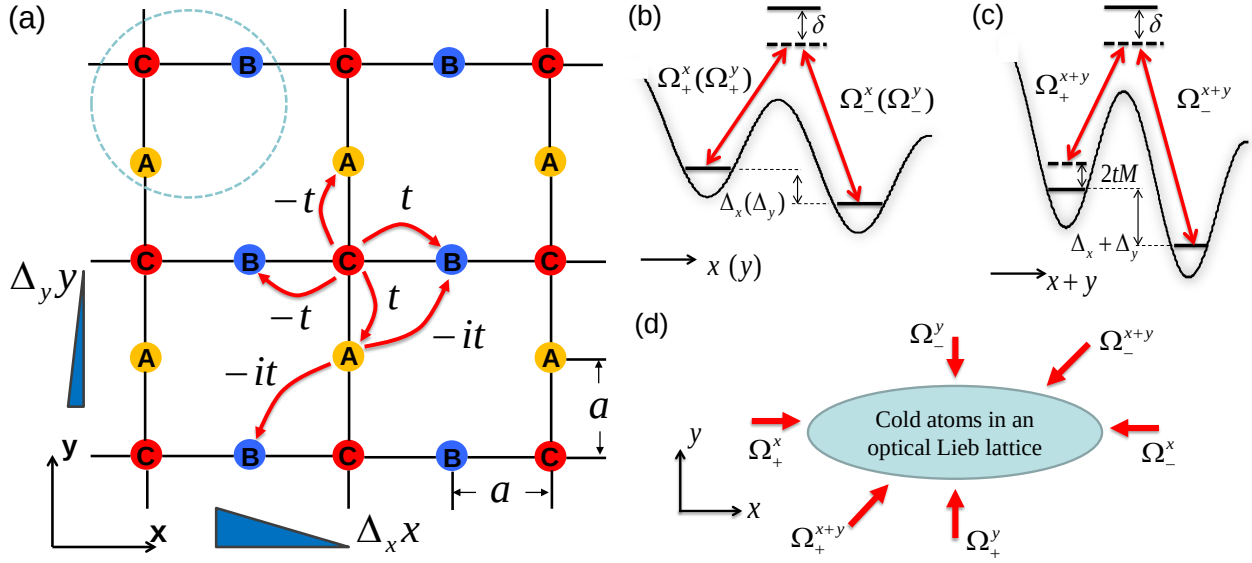

FIG. S8: (Color online) (a) Schematic diagram of realizing 2D Maxwell points and Maxwell quasiparticles in an optical Lieb lattice. A unit cell indicated by dashed line is composed of three sites labeled by A, B, C, with the lattice constant a. The three sublattices form the pseudospin-1 basis, and the spin-flip hopping along each direction with the corresponding hopping amplitude is shown. These hopping can be realized by the Raman-assisted hopping method with the help of the linear title potentials $\Delta_x x$ and $\Delta_y y$ and the application of laser beams, similar as the scheme in the square optical lattice. (b) Two pairs of Raman beams for inducing the desired hopping along x and y directions; (c) A pair of Raman beams for inducing the desired hopping along $x+y$ direction and a two-photon detuning for inducing the constant term $2tM\hat{S}_z$; (d) The total lasers with the corresponding propagation direction.

optical Lieb lattice [6]. In experiments, the optical Lieb lattice for cold atoms has been constructed by superimposing three types of optical lattices, with the tunable optical potential [6]

$$\begin{aligned} V(x,y) = &- V^x_{\rm long}\cos^2(k_L x) - V^y_{\rm long}\cos^2(k_L y) - V^x_{\rm short}\cos^2(2k_L x) \\ &- V^y_{\rm short}\cos^2(2k_L y) - V_{\rm diag}\cos^2\left[2k_L(x-y)+\frac{\pi}{2}\right]. \end{aligned} \tag{S.15}$$

Here $k_L = 2\pi/\lambda$ is a wave number of a long lattice with a depth $V_{\rm long}$, a short lattice $V_{\rm short}$ is formed by laser beams at wave length $\lambda/2$, and a diagonal lattice $V_{\rm diag}$ with the wave number $\sqrt{2}k_L$ is realized by interference of the mutually orthogonal laser beams at λ along the x and y directions. The optical Lieb lattice system is shown in Fig. S8(a), with three sublattices A, B, C forming a unit cell. By tuning the lattice depths $\{V_{\rm long}, V_{\rm short}, V_{\rm diag}\}$, one can change the energy of the sublattices [6].

In this system, the pseudospin-1 basis are replaced by the three sublattices in a unit cell, and thus the three spin states are given by

$$|A\rangle \Longleftrightarrow |\uparrow\rangle,\ |B\rangle \Longleftrightarrow |0\rangle,\ |C\rangle \Longleftrightarrow |\downarrow\rangle. \tag{S.16}$$

In this lattice, the spin-flip hopping $|B\rangle \leftrightarrow |C\rangle$ and $|A\rangle \leftrightarrow |C\rangle$ under the operators $\hat{S}_x$ and $\hat{S}_y$ along the x and y axis become naturally the nearest neighbor hopping in that axis, with the corresponding hopping amplitudes are shown in Fig. S8(a). With the similar Raman-assisted hopping method, the hopping along the x axis and the y axis can be realized by two pairs of laser beams, $\Omega^x_\pm = \Omega_0 e^{\pm ik_1 x}$ and $\Omega^y_\pm = \pm\Omega_0 e^{\pm ik_1 y}$, under the large linear title potentials $\Delta_x x$ and $\Delta_y y$, respectively, as shown in Fig. S8(b). The detuning in each direction matches the frequency offset of the corresponding Raman beams as we can choose the title energies $\Delta_x \approx 2.5\Delta_y$ with $\Delta_y \gg t_0$ being assumed. In this system, since only one atomic internal state is used in the Raman transitions, then one can address the atoms only through the energy selection without involving the laser polarization [3, 4]. Under the two pairs of laser beams, the momenta transferred in the Raman transition along the x and y directions are $\delta\mathbf{k}_1 = -2k_1\hat{x}$ and $\delta\mathbf{k}_2 = -2k_2\hat{y}$, respectively. Thus the corresponding site-dependent hopping phases along x and y directions are $e^{-2ik_1 x} = e^{-2ik_1 j_x a}$ and $e^{-2ik_2 y} = e^{-2ik_2 j_y a}$, with the lattice site index (j_x, j_y). We can choose the parameters $k_1 = k_2 = \pi/2a$ to induce the hopping phases $e^{-i\pi j_x} = e^{-i\pi j_y} = 0, \pi$ staggered along the x and y directions, which lead to the desired hopping $|B\rangle \leftrightarrow |C\rangle$ and $|A\rangle \leftrightarrow |C\rangle$ in the corresponding axis.

The spin-flip hopping $|A\rangle \leftrightarrow |B\rangle$ under the operator $\hat{S}_z$ in this lattice becomes next-nearest neighbor hopping along the $x+y$ or $x-y$ axis, with the corresponding hopping amplitude along the $x+y$ axis is shown in Fig. S8(a). This hopping can be achieved by additional Raman transition by using the third pair of lasers $\Omega^{x+y}_+ = \Omega_0 e^{ik_3(x+y)}$ and $\Omega^{x+y}_- = -i\Omega_0 e^{-ik_3(x+y)}$ with a different matching energy $\Delta_x + \Delta_y = 3.5\Delta_y$, as shown in Fig. S8(c). Here a two-photon detuning in the transition can be used to induce the constant term $2tM\hat{S}_z$, without adding other coupling beams in this system. We choose the parameter $k_3 = \pi/a$, then the site dependent phase along the $x+y$ direction can always be reduced to $e^{-2ik_3(j_x+j_y)a} = 1$, such that the hopping constant $-it$ along this direction is achieved by the two Raman beams. If the hopping $|A\rangle \leftrightarrow |B\rangle$ along the $x-y$ axis is wanted, one can also add the Raman transition with the matching energy $\Delta_x - \Delta_y = 1.5\Delta_y$. The laser configuration of this system is shown in Fig. S8(d). Under these conditions, the Bloch Hamiltonian of the 2D Maxwell systems now becomes

$$\begin{aligned} \mathcal{H}(\mathbf{k}) =& R_x(\mathbf{k})\hat{S}_x + R_y(\mathbf{k})\hat{S}_y + R_z(\mathbf{k})\hat{S}_z, \\ R_x =& 2t\sin k_x,\ R_y = 2t\sin k_y,\ R_z = 2t[M - \cos(k_x + k_y)]. \end{aligned} \tag{S.17}$$

Here the spin-1 matrices $\hat{S}_{x,y,z}$ acts on the three sublattices and the lattice constant $a \equiv 1$. In this case, one can obtain the Maxwell points and the associated Maxwell quasiparticles, similar as the case discussed in the main text. For instance, when the parameter $M = 1$, there is a Maxwell point at $\mathbf{K} = (0,0)$ with the low-energy effective Hamiltonian $\mathcal{H}_{\rm eff}(\mathbf{q}) \approx vq_x\hat{S}_x + vq_y\hat{S}_y$, where $v = 2t$ is the effective speed of light and $\mathbf{q} = \mathbf{k} - \mathbf{K}$.

DERIVATION OF THE TOPOLOGICAL INVARIANTS

The Berry curvature is given by $\mathbf{F} = \nabla\times\mathbf{A}$, where the Berry connection $\mathbf{A} = -i\langle\psi|\nabla\psi\rangle$. For the Bloch Hamiltonian of the 2D model in the main text $\mathcal{H} = \mathbf{R}(\mathbf{k})\cdot\mathbf{S}$, the Berry connection $\mathbf{A} = (A_x, A_y, 0)$ for the lowest band with the energy $E = -R$ is given by [7]

$$A_\mu = -\frac{R_3}{R(R^2 - R_3^2)}\left(R_2\frac{\partial R_1}{\partial k_\mu} - R_1\frac{\partial R_2}{\partial k_\mu}\right). \tag{S.18}$$

The corresponding Berry curvature is $\mathbf{F}=(0,0,F_{xy})$ with F_{xy} being given by

$$F_{xy}=\frac{\partial A_y}{\partial k_x}-\frac{\partial A_x}{\partial k_y}=-\frac{1}{R^3}\varepsilon_{abc}R_a\frac{\partial R_b}{\partial k_x}\frac{\partial R_c}{\partial k_y}=-\frac{1}{R^3}\mathbf{R}\cdot(\frac{\partial \mathbf{R}}{\partial k_x}\times\frac{\partial \mathbf{R}}{\partial k_y}), \tag{S.19}$$

where the Bloch vectors are $R_x=2t\sin k_x$, $R_y=2t\sin k_y$, and $R_z=2t(M-\cos k_x-\cos k_y)$. A straightforward calculation gives the following form

$$F_{xy}=\frac{\cos k_x+\cos k_y-M\cos k_x\cos k_y}{(\sin^2 k_x+\sin^2 k_y+(M-\cos k_x-\cos k_y)^2)^{3/2}}. \tag{S.20}$$

We can thus obtain the Chern number for this band

$$\mathcal{C}=\frac{1}{2\pi}\oint_S d\mathbf{k}\cdot\mathbf{F}(\mathbf{k})=\frac{1}{2\pi}\oint_S d^2kF_{xy}=\begin{cases}2\text{sign}(M), & 0<|M|<2\\ 0, & |M|>2\end{cases} \tag{S.21}$$

For $M=\pm 2$, we respectively expand the Hamiltonian around $\mathbf{K}_+=(0,0)$ and $\mathbf{K}_-=(\pi,\pi)$, and obtain the low-energy effective Hamiltonian

$$H_\pm(\mathbf{q})=\pm(vq_x\hat{S}_x+vq_y\hat{S}_y-2tm\hat{S}_z), \tag{S.22}$$

where $m=2\mp M$, $v=2t$, and $\mathbf{q}=\mathbf{k}-\mathbf{K}_\pm$ with $|\mathbf{q}|\ll|\mathbf{k}|$. We can obtain the effective Berry curvature

$$F_{xy}=\pm\frac{m}{(q^2+m^2)^{3/2}}, \tag{S.23}$$

where $q=\sqrt{q_x^2+q_y^2}$. Thus the Berry phase γ integrated around the Maxwell point $\mathbf{K}_\pm$ for the Fermi surface (FS) can be derived by

$$\gamma=\oint_{FS}d\mathbf{k}\cdot\mathbf{A}(\mathbf{k})=\pm\oint_{FS}d^2q\frac{m}{(q^2+m^2)^{3/2}}=\pm\int_0^{2\pi}d\theta\int_0^{k_F}\frac{m}{(q^2+m^2)^{3/2}}qdq=\pm 2\pi\int_0^{k_F}\frac{m}{(q^2+m^2)^{3/2}}qdq, \tag{S.24}$$

where k_F is the Fermi momentum and the parameter $m\to 0$. Let $q=m\tan\varphi$, then we have $1+\tan^2\varphi=\sec^2\varphi$ and $dq=m\sec^2\varphi d\varphi$. Substituting these relationships into the above equation, we obtain γ as a function of m:

$$\begin{aligned}\gamma&=\pm 2\pi\int_0^{k_F}\frac{m}{(q^2+m^2)^{3/2}}qdq=\pm 2\pi\int_0^{\varphi_F}\frac{m^2\tan^2\varphi}{m^3\sec^3\varphi}m\sec^2\varphi d\varphi\\&=\pm 2\pi\int_0^{\varphi_F}\sin\varphi d\varphi=\pm 2\pi(-\cos\varphi)|_0^{\varphi_F}=\pm 2\pi(-\frac{m}{\sqrt{q^2+m^2}})|_0^{k_F}\\&=\pm 2\pi(1-\frac{m}{\sqrt{k_F^2+m^2}}).\end{aligned} \tag{S.25}$$

Thus for $m=0$, we obtain $\gamma=\pm 2\pi$ for $M=\pm 2$.

For $M=0$, we respectively expand the Hamiltonian around $\mathbf{K}_{(0,\pi)}=(0,\pi)$ and $\mathbf{K}_{(\pi,0)}=(\pi,0)$,and obtain the low-energy effective Hamiltonian

$$\mathcal{H}_0(\mathbf{q})=\pm(vq_x\hat{S}_x-vq_y\hat{S}_y+2tm_0\hat{S}_z) \tag{S.26}$$

where $m_0=\pm M$ in this case, and $\mathbf{q}=\mathbf{k}-\mathbf{K}_{(0,\pi)/(\pi,0)}$, $|\mathbf{q}|\ll|\mathbf{k}|$. We can obtain the Berry connection

$$A_x=\pm\frac{m_0q_y}{q^2\sqrt{q^2+m_0^2}},\ A_y=\pm\frac{m_0q_x}{q^2\sqrt{q^2+m_0^2}}. \tag{S.27}$$

Thus the Berry phase γ integrated around the Maxwell point $\mathbf{K}_{(0,\pi)/(\pi,0)}$ for Fermi surface can be derived as

$$\begin{aligned}\gamma&=\oint_{FS}d\mathbf{k}\cdot\mathbf{A}(\mathbf{k})=\int_0^{2\pi}k_Fd\theta A_\theta=\int_0^{2\pi}k_Fd\theta(A_y\frac{q_x}{k_F}-A_x\frac{q_y}{k_F})\\&=\pm\frac{m_0}{\sqrt{k_F^2+m_0^2}}\int_0^{2\pi}(\cos^2\theta-\sin^2\theta)d\theta=\pm\frac{m_0}{\sqrt{k_F^2+m_0^2}}\int_0^{2\pi}d\theta\cos(2\theta)=0,\end{aligned} \tag{S.28}$$

where we have used the relationships $q_x=k_F\cos\theta$ and $q_y=k_F\sin\theta$.

A SCHEME TO DETECT THE TOPOLOGICAL CHERN NUMBER

Now we propose a practical method to directly measure the Chern number in our systems, based on a generalization of topological pumping in optical lattices [8–12]. We start with the original definition of the Chern number, which is given by

$$\mathcal{C} = \frac{1}{2\pi}\oint dkA(\mathbf{k}) = \frac{1}{2\pi}\int_{-\pi}^{\pi} dk_y \partial_{k_y}\int_{-\pi}^{\pi} dk_x A(k_x,k_y) = \frac{1}{2\pi}\int_{-\pi}^{\pi} dk_y \partial_{k_y}\varphi_{Zak}(k_y) \tag{S.29}$$

where $A(k) = -i\langle u(k)|\partial_k|u(k)\rangle$ is the Berry connection, and the Zak phase for a reduced 1D system is $\varphi_{Zak} = \int_{-\pi}^{\pi} dkA(k) = 2\pi\langle w|\hat{x}|w\rangle = 2\pi\langle n_x\rangle$. Here $|w\rangle$ denotes the Wannier functions. We can obtain the Chern number of our 2D Maxwell insulators

$$\mathcal{C} = \int_{-\pi}^{\pi} dk\partial_{k_y}\langle n_x(k_y)\rangle \tag{S.30}$$

$\langle n_x(k_y)\rangle$ is the center of hybrid Wannier function (HWF) [9–12]. The HWF center for tight-binding chain in our system with lattice site L_x under open boundary condition is given by

$$\langle n_x(k_y)\rangle = \frac{\sum_{i_x} i_x\rho(i_x,k_y)}{\sum_{i_x}\rho(i_x,k_y)} \tag{S.31}$$

where i_x is the lattice-site index, and $\rho(i_x,k_y)$ is the density of the HWF and denotes the atomic densities resolved along x direction as a function of k_y. Here, the hybrid density can be written as

$$\rho(i_x,k_y) = \sum_{occupied\ states} |i_x,k_y\rangle\langle i_x,k_y|, \tag{S.32}$$

where $|i_x,k_y\rangle$ is the hybrid eigenstates of the system. We can prove that the Chern number can be obtained from the shift of the HWF:

$$\mathcal{C} = \sum_j \Delta\langle n_x(k_y(j))\rangle \tag{S.33}$$

where $\Delta\langle n_x(k_y(j))\rangle$ represent the difference of the HWF center $\langle n_x\rangle$ at the jump discontinuity $k_y(j)$, j is the number of jump discontinuity for $\langle n_x\rangle$, the sum of the difference at all jump points is equal to the Chern number.

Prove: Due to the system is under period boundary condition, $\langle n_x(\pi)\rangle = \langle n_x(-\pi)\rangle$.

1. While $j = 0$, $\langle n_x\rangle$ is continuous.

$$\mathcal{C} = \int_{-\pi}^{\pi} dk_y\partial_{k_y}\langle n_x(k_y)\rangle = \int_{-\pi}^{\pi} d\langle n_x(k_y)\rangle = \langle n_x(k_y)\rangle|_{-\pi}^{\pi} = 0$$

2. While $j \neq 0$, $\langle n_x\rangle$ is discontinuous. For simply, we suppose function $f(x)$ have j times jump discontinuities, divided $f(x)$ into $j+1$ segment, and satisfied $f(x_0) = f(x_{j+1})$, $x(j)$ is the jump discontinuity. Then we have

$$\begin{aligned}
\int_{x_0}^{x_{j+1}} dx\partial_x f(x) &= \int_{x_0}^{x_{j+1}} df(x) = \int_{x_0}^{x_1} df(x) + \int_{x_1}^{x_2} df(x) + \int_{x_2}^{x_3} df(x) + \cdots + \int_{x_{j-1}}^{x_j} df(x) + \int_{x_j}^{x_{j+1}} df(x) \\
&= f(x)|_{x_0}^{x_1} + f(x)|_{x_1}^{x_2} + f(x)|_{x_2}^{x_3} + \cdots + f(x)|_{x_{j-1}}^{x_j} + f(x)|_{x_j}^{x_{j+1}} \\
&= f(x_1)' - f(x_0) + f(x_2)' - f(x_1) + f(x_3)' - f(x_2) + \cdots + f(x_j)' - f(x_{j-1}) + f(x_{j+1}) - f(x_j) \\
&= f(x_{j+1}) - f(x_0) + f(x_1)' - f(x_1) + \cdots + f(x_j)' - f(x_j) = \sum_j (f(x_j)' - f(x_j))
\end{aligned}$$

where $f(x_j)'$ and $f(x_j)$ are belong to the jth and $(j+1)$th segment of $f(x)$ at jth jump discontinuity, respectively.

According to these results, we describe a scheme to directly detect the Chern number based on a generalization of topological pumping in optical lattices [8–12]. Our 2D insulating Hamiltonian can be viewed as a fictitious 1D insulator subject to an external parameter k_y, and we also know the polarization of this 1D insulator can be expressed by means of the center of the HWFs [9–12], which are localized in the x axis retaining Bloch character in the k_y

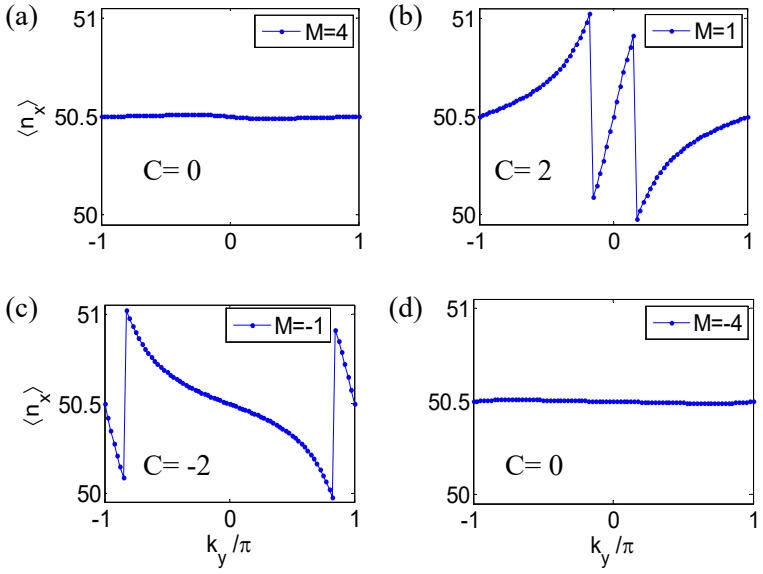

FIG. S9: (Color online) The HWF centers in a tight-binding chain of length $L_x = 100$ at 1/3 filling as a function of the adiabatic pumping parameter k_y for different parameters M. There is no jump of $\langle n_x(k_y)\rangle$ in (a) and (d), which is consistent with the expected $\mathcal{C} = 0$ for $M > 2$ and $M < -2$ in these cases. In (b) and (c), $\langle n_x(k_y)\rangle$ both show the jump of two unit cell for $M = 1$ and $M = -1$, corresponding to nontrivial cases with $\mathcal{C} = 2$ and $\mathcal{C} = -2$, respectively.

dimension in our case. This polarization is a function of k_y, which acts as an external parameter under which the polarization changes. When k_y is adiabatically changed by 2π, the change in polarization, i.e., the shift of the HWF center, is proportional to the Chern number. This is a manifestation of topological pumping [8], with k_y being the adiabatic pumping parameter. In Fig. S9, we numerically calculate $\langle n_x(k_y)\rangle$ in a tight-binding chain of length $L_x = 100$ at 1/3 filling (assuming the Fermi energy $E_F = 0$). For the case in Figs. S9(a) and S9(d), $\langle n_x(k_y)\rangle$ shows no jump, which are consistent with the expected $\mathcal{C} = 0$ for the trivial case $M = 4$ and $M = -4$. The results for $M = 1$ in Fig. S9(b) shows two discontinuous jumps of one unit cell, indicating that a particle is pumped across the system [11, 12], the Chern number for this case is $\mathcal{C} = 2$, and the result in Fig. S9(c) is similar to Fig. S9(b) but with opposite jump direction and Chern number for $M = -1$. This establishes a direct and clear connection between the shift of the hybrid density center and the topological invariant.

In cold atom experiments, the atomic density $\rho(i_x, k_y)$ can be directly measured by the hybrid time-of-flight images [9], which is referring to an *in situ* measurement of the density distribution of the atomic cloud in the x direction during free expansion along the y direction. In the measurement, the optical lattice is switched off along the y direction while keeping the system unchanged in the x direction. One can map out the crystal momentum distribution along k_y in the time-of-flight images and a real space density resolution in the x direction can be done at the same time. Thus one can directly extract Chern number from this hybrid time-of-fight images in the cold atom system.

* Electronic address: zdanwei@126.com
† Electronic address: slzhu@nju.edu.cn

[1] R. Good and T. Nelson, *Classical Theory of Electric and Magnetic Fields* (Academic Press, New York, 1971)
[2] R. Oppenheimer, Phys. Rev. **38**, 725 (1931)
[3] D. Jaksch and P. Zoller, New J. Phys. **5**, 56 (2003); J. Dalibard, F. Gerbier, G. Juzeliūnas, and P. Öhberg, Rev. Mod. Phys. **83**, 1523 (2011); N. Goldman, G. Juzeliūnas, P. Öhberg, and I. B. Spielman, Rep. Prog. Phys. **77**, 126401 (2014).
[4] H. Miyake, G. A. Siviloglou, C. J. Kennedy, W. C. Burton, and W. Ketterle, Phys. Rev. Lett. **111**, 185302 (2013); M. Aidelsburger, M. Atala, M. Lohse, J. T. Barreiro, B. Paredes, and I. Bloch, Phys. Rev. Lett. **111**, 185301 (2013).
[5] S.-T. Wang, D.-L. Deng, and L.-M. Duan, Phys. Rev. Lett. **113**, 033002 (2014).
[6] S. Taie, H. Ozawa, T. Ichinose, T. Nishio, S. Nakajima, and Y. Takahashi, Sci. Adv. **1**, 1500854 (2015).
[7] Y. He, J. Moore, and C. M. Varma, Phys. Rev. B **85**, 155106 (2012).
[8] D. J. Thouless, Phys.Rev. B **27**, 6083 (1983); Q. Niu, Phys. Rev. Lett. **64**, 1812 (1990).
[9] L. Wang, A. A. Soluyanov, and M. Troyer, Phys. Rev. Lett. **110**, 166802 (2013); L. Wang, M. Troyer, and X. Dai, Phys.

Rev. Lett. **111**, 026802 (2013).
[10] D.-W. Zhang, S.-L. Zhu, and Z. D. Wang, Phys. Rev. A **92**, 013632 (2015).
[11] R. D. King-Smith and D. Vanderbilt, Phys. Rev. B **47**, 1651 (1993); S. Coh and D. Vanderbilt, Phys. Rev. Lett. **102**, 107603 (2009).
[12] N. Marzari, A. Mostofi, J. R. Yates, I. Souza, and D. Vanderbilt, Rev. Mod. Phys. **84**, 1419 (2012).